

## A CHANDRASEKHAR MASS PROGENITOR FOR THE TYPE IA SUPERNOVA REMNANT 3C 397 FROM THE ENHANCED ABUNDANCES OF NICKEL AND MANGANESE

HIROYA YAMAGUCHI<sup>1,2,3</sup>, CARLES BADENES<sup>4</sup>, ADAM R. FOSTER<sup>3</sup>, EDUARDO BRAVO<sup>5</sup>, BRIAN J. WILLIAMS<sup>1</sup>,  
KEIICHI MAEDA<sup>6,7</sup>, MASAYOSHI NOBUKAWA<sup>8</sup>, KRISTOFFER A. ERIKSEN<sup>9</sup>, NANCY S. BRICKHOUSE<sup>3</sup>,  
ROBERT PETRE<sup>1</sup>, KATSUJI KOYAMA<sup>8,10</sup>

*Draft version August 6, 2018*

### ABSTRACT

Despite decades of intense efforts, many fundamental aspects of Type Ia supernova (SNe Ia) remain elusive. One of the major open questions is whether the mass of the exploding white dwarf (WD) is close to the Chandrasekhar limit. Here we report the detection of strong K-shell emission from stable Fe-peak elements in the *Suzaku* X-ray spectrum of the Type Ia supernova remnant (SNR) 3C 397. The high Ni/Fe and Mn/Fe mass ratios (0.11–0.24 and 0.018–0.033, respectively) in the hot plasma component that dominates the K-shell emission lines indicate a degree of neutronization in the SN ejecta which can only be achieved by electron captures in the dense cores of exploding WDs with a near-Chandrasekhar mass. This suggests a single-degenerate origin for 3C 397, since Chandrasekhar mass progenitors are expected naturally if the WD accretes mass slowly from a companion. Together with other results supporting the double-degenerate scenario, our work adds to the mounting evidence that both progenitor channels make a significant contribution to the SN Ia rate in star-forming galaxies.

*Subject headings:* atomic data — infrared: ISM — ISM: individual objects (3C 397, G41.1–0.3) — ISM: supernova remnants — nuclear reactions, nucleosynthesis, abundances — X-rays: ISM

### 1. INTRODUCTION

Type Ia supernovae (SNe Ia) are widely believed to result from the thermonuclear explosion of a carbon-oxygen white dwarf (WD) that is destabilized by mass transfer in a binary system (e.g., Maoz et al. 2014). Even though their use as distance indicators in cosmology has sparked considerable interest in SNe Ia (e.g., Riess et al. 1998; Perlmutter et al. 1999), many fundamental aspects of these explosions remain obscure. Two major channels are thought to lead to SN Ia explosions: the single degenerate (SD) scenario (Whelan & Iben 1973) where a WD accretes matter from a non-degenerate companion and explodes when its mass grows close to the Chandrasekhar limit ( $M_{\text{Ch}} \approx 1.4 M_{\odot}$ ), and the double degenerate (DD) scenario (Webbink 1984) where the ex-

plosion is triggered by the dynamical merger of two WDs. Unfortunately, the remarkable uniformity in SN Ia light curves and spectra makes it difficult to infer the properties of the progenitors from the explosions themselves. Because of this, most observational efforts to distinguish between progenitor scenarios for individual SNe Ia have focused on searches for circumstellar material (Patat et al. 2007; Sternberg et al. 2011; Badenes et al. 2007; Williams et al. 2011, 2014) or pre-existing/surviving stellar companions (Li et al. 2011; González Hernández et al. 2012; Schaefer & Pagnotta 2012).

From the point of view of the SN nucleosynthesis, the main difference between SD and DD systems is the central density of the WD at the onset of the thermonuclear runaway (Pakmor et al. 2012; Seitzzahl et al. 2013a). In SD progenitors, the exploding WD should always be close to  $M_{\text{Ch}}$ , and have a dense ( $\rho \gtrsim 2 \times 10^8 \text{ g cm}^{-3}$ ) core where electron captures can take place efficiently, leading to significant production of neutronized species like  $^{58}\text{Ni}$  and  $^{55}\text{Mn}$  (Iwamoto et al. 1999; Seitzzahl et al. 2013b). In contrast, the DD explosion scenarios that can best reproduce the observed properties of SNe Ia require lower masses and central densities for the primary WD, and therefore predict lower yields of these species (Pakmor et al. 2012; van Kerkwijk 2013). For this reason, the yield of  $^{58}\text{Ni}$ ,  $^{55}\text{Mn}$ , and other neutronized species has been identified as a powerful diagnostic for SN Ia progenitors (Maeda et al. 2010a; Seitzzahl et al. 2015). However, a combination of long half-lives and complex ionization issues at play in nebular spectra (Dessart et al. 2014) makes it extremely difficult to quantify these yields for individual objects during the optical SN phase (Mazzali et al. 2007; Gerardy et al. 2007; Maeda et al. 2010b).

X-ray observations of evolved supernova remnants

Electronic address: hiroya.yamaguchi@nasa.gov

<sup>1</sup> NASA Goddard Space Flight Center, Code 662, Greenbelt, MD 20771, USA

<sup>2</sup> Department of Astronomy, University of Maryland, College Park, MD 20742, USA

<sup>3</sup> Harvard-Smithsonian Center for Astrophysics, 60 Garden Street, Cambridge, MA 02138, USA

<sup>4</sup> Department of Physics and Astronomy and Pittsburgh Particle Physics, Astrophysics and Cosmology Center (PITT PACC), University of Pittsburgh, 3941 O'Hara St, Pittsburgh, PA 15260, USA

<sup>5</sup> E.T.S. Arquitectura del Vallès, Universitat Politècnica de Catalunya, Carrer Pere Serra 1-15, 08173 Sant Cugat del Vallès, Spain

<sup>6</sup> Department of Astronomy, Kyoto University, Kitashirakawa-oiwake-cho, Sakyo-ku, Kyoto 606-8502, Japan

<sup>7</sup> Kavli Institute for the Physics and Mathematics of the Universe (WPI), University of Tokyo, 5-1-5 Kashiwanoha, Kashiwa, Chiba 277-8583, Japan

<sup>8</sup> Department of Physics, Kyoto University, Kitashirakawa-oiwake-cho, Sakyo-ku, Kyoto 606-8502, Japan

<sup>9</sup> Theoretical Design Division, Los Alamos National Laboratory, PO Box 1663, Los Alamos, NM 87545, USA

<sup>10</sup> Department of Earth and Space Science, Osaka University, 1-1 Machikaneyama, Toyonaka, Osaka 560-0043, Japan

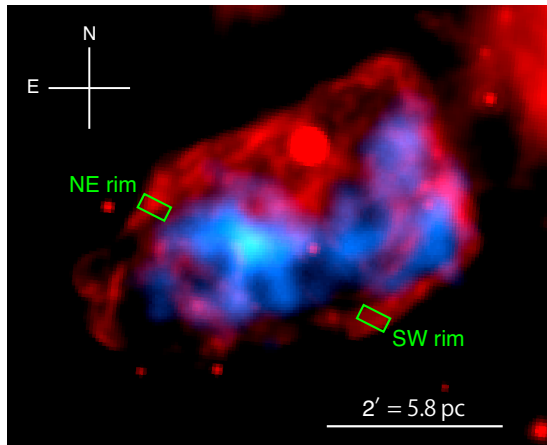


**Figure 1.** Two-color image of SNR 3C 397. Red and blue represent 24  $\mu\text{m}$  IR (*Spitzer*) and 5–9 keV X-rays (*Suzaku*), respectively. The green rectangles indicate the locations where the IR spectra (Fig. 2a) are extracted.

(SNRs) offer an excellent opportunity to make robust measurements of the yields of neutronized species, as the innermost ejecta must have been thermalized by the reverse shock in the SNRs, and will therefore be visible in the X-ray spectrum. 3C 397 (G41.1–0.3) is an ideal target in this sense, since it is dynamically more evolved than other well-known Type Ia SNRs (i.e., Kepler, Tycho, SN 1006). Although 3C 397 has sometimes been classified as a core-collapse SNR due to its proximity to molecular clouds (Safi-Harb et al. 2000), most studies, including our own systematic analysis of Fe K-shell emission in young and middle-aged SNRs, agree on a Type Ia origin (e.g., Chen et al. 1999; Yang et al. 2013; Yamaguchi et al. 2014a). Here we present strong evidence for the presence of electron capture products in the X-ray spectrum of 3C 397, after proving that the SNR is indeed evolved. In our analysis, we assume the distance to the SNR to be 10 kpc (Safi-Harb et al. 2000, and references therein), but our main results and conclusions are not affected by the uncertainty in the distance estimate.

The errors quoted in the text and table, and the error bars in the figures are at the  $1\sigma$  confidence level, unless otherwise stated.

## 2. OBSERVATIONAL RESULTS

We analyzed archival *Spitzer* infrared (IR) and *Suzaku* X-ray data from 3C 397. The IR observations were performed using the Multiband Imaging Photometer (MIPS) and the Infrared Spectrograph (IRS) during April 2005. The X-ray observation was performed in October 2010 with a total effective exposure of 69 ks for the X-ray Imaging Spectrometer (XIS). We followed the standard procedures for data reduction. Figure 1 shows a composite image of 3C 397 in the 24  $\mu\text{m}$  IR (red) and 5–9 keV X-rays (blue).

### 2.1. IR Spectroscopy

In young SNRs, mid-IR continuum emission arises from dust grains in the interstellar medium (ISM) that are heated in the post-shock gas by collisions with energetic ions and electrons. Therefore, IR spectra can constrain the density and mass of the swept-up ambient medium (e.g., Borkowski et al. 2006). Figure 2a

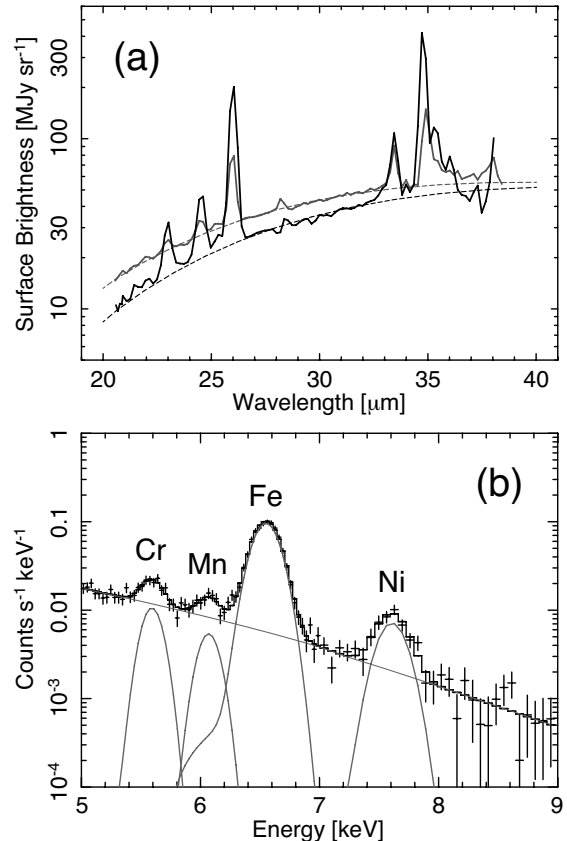


**Figure 2.** (a) *Spitzer* IRS spectra used to measure the ambient density. Black and gray data are taken from the NE and SW rims indicated in Figure 1, respectively. The continuum components are fitted with a dust emission model (dashed curves). (b) Spatially integrated *Suzaku* XIS spectrum of 3C 397. The model (gray lines) consists of a bremsstrahlung continuum with an electron temperature of  $\log_{10}(T_e [\text{K}]) = 7.39 \pm 0.04$  and four Gaussians with the parameters listed in Table 1.

shows the background-subtracted *Spitzer* IRS spectra from the two regions indicated in Figure 1. Using the dust emission models and analysis procedures described in Borkowski et al. (2006) and Williams et al. (2012), we fitted the 21–33  $\mu\text{m}$  continuum and derived post-shock proton number densities of  $4.6 \pm 0.4 \text{ cm}^{-3}$  and  $8.5 \pm 0.8 \text{ cm}^{-3}$  for the NE and SW rims, respectively. The average pre-shock density is therefore  $\rho_0 = \mu_{\text{H}} \times (4.6 + 8.5)/2 \times (1/4) \approx 3.8 \times 10^{-24} \text{ g cm}^{-3}$ , where  $\mu_{\text{H}} = 1.4 \times 1.67 \times 10^{-24} \text{ g}$  is the mean mass per hydrogen nucleus for solar abundances (Asplund et al. 2009).

The spatially-integrated IR flux from the SNR is  $\sim 20 \text{ Jy}$ , which requires a swept-up dust mass of  $\sim 0.2 M_{\odot} d_{10}^2$ . This estimate accounts for the fact that the mid-IR observations usually capture only  $\sim 20\%$  of the flux in this band, because the rest of the dust is colder and emits at longer wavelengths (Borkowski et al. 2006; Williams et al. 2014). Taking the standard dust-to-gas ratio in the Milky Way (Weingartner & Draine 2001), the estimated dust mass leads to a swept-up gas mass of  $\sim 25 M_{\odot} d_{10}^2$ . The SNR shape can be well approximated by a  $2/4 \times 1/3 \times 1/3$  ellipsoid, corresponding to a volume of  $1.4 \times 10^{58} d_{10}^3 \text{ cm}^3$ . The average ambient density that the SNR blast wave has experienced is therefore

**Table 1**

The best-fit spectral parameters, theoretically-predicted line emissivities and their ratios, and derived mass ratios for the Fe-peak elements observed in the hard (5–9 keV) X-ray spectrum of 3C 397.

|                                 | Centroid<br>(eV)                               | FWHM<br>(eV)                      | Flux<br>(photons cm <sup>-2</sup> s <sup>-1</sup> )     | Emissivity<br>(10 <sup>-13</sup> photon cm <sup>3</sup> s <sup>-1</sup> ) | $\varepsilon/\varepsilon_{\text{Fe}}$ | $M/M_{\text{Fe}}$                         |
|---------------------------------|--|-----------------------------------|---|---|---------------------------------------|---|
| Cr K $\alpha$                   | 5596 <sup>+12</sup> <sub>-11</sub> ( $\pm 6$ ) | 104 <sup>+45</sup> <sub>-64</sub> | 1.05 <sup>+0.15</sup> <sub>-0.14</sub> $\times 10^{-5}$ | 3.3 <sup>+1.1</sup> <sub>-1.0</sub>                                       | 2.6 $\pm$ 0.2                         | 0.027 <sup>+0.007</sup> <sub>-0.006</sub> |
| Mn K $\alpha$                   | 6073 <sup>+19</sup> <sub>-20</sub> ( $\pm 6$ ) | 104                               | 5.75 <sup>+1.17</sup> <sub>-1.10</sub> $\times 10^{-6}$ | 2.2 $\pm$ 0.7   | 1.7 $\pm$ 0.1                         | 0.025 <sup>+0.008</sup> <sub>-0.007</sub> |
| Fe K $\alpha$                   | 6556 <sup>+3</sup> <sub>-2</sub> ( $\pm 7$ )   | 181 $\pm$ 6                       | 1.38 $\pm$ 0.03 $\times 10^{-4}$                        | 1.3 <sup>+0.5</sup> <sub>-0.4</sub>                                       | 1                                     | 1   |
| Ni K $\alpha$ (+ Fe K $\beta$ ) | 7616 $\pm$ 13 ( $\pm 8$ )                      | 197 <sup>+46</sup> <sub>-47</sub> | 1.61 <sup>+0.18</sup> <sub>-0.17</sub> $\times 10^{-5}$ | —   | —                                     | —   |
| Ni K $\alpha$                   | —  | —                                 | 1.09 <sup>+0.34</sup> <sub>-0.30</sub> $\times 10^{-5}$ | 0.64 <sup>+0.26</sup> <sub>-0.22</sub>                                    | 0.49 $\pm$ 0.03                       | 0.17 <sup>+0.07</sup> <sub>-0.05</sub>    |

**Note.** — The uncertainties in parenthesis are the systematic component (0.1% of the mean energy; Ozawa et al. 2009). The width (FWHM) of the Mn K $\alpha$  line was linked to that of Cr K $\alpha$ . The line emissivity  $\varepsilon$  is defined as  $F = \varepsilon n_e n_{\text{ion}} V / (4\pi D^2)$ , where  $F$ ,  $n_{\text{ion}}$ ,  $V$ , and  $D$ , are the line flux, ion number density, emitting volume, and distance to the SNR, respectively. The Ni K $\alpha$  emission observed in the X-ray spectrum (Fig. 2b) is in fact contributed by Fe K $\beta$  lines as well, with their centroids overlapping with each other (see text for details). The Ni K $\alpha$  flux and Ni/Fe mass ratio given in the last row are obtained after subtracting the Fe K $\beta$  contribution.

estimated to be  $3.6 \times 10^{-24} d_{10}^{-1} \text{ g cm}^{-3}$ , consistent with (and independent from) the measurement from the IR spectra at the nominal distance to the SNR. Because the total swept-up mass ( $\sim 25 M_{\odot}$ ) is much larger than the typical SN Ia ejecta mass, we conclude that the reverse shock must have thermalized the innermost ejecta (e.g., Truelove & McKee 1999).

## 2.2. X-Ray Spectroscopy

Given the ISM origin of the IR emission, the clear anticorrelation between the IR and X-ray morphologies (Fig. 1) suggests that the hard X-rays predominantly originate from the ejecta. The spectrum of the *Suzaku* XIS in the 5–9 keV band extracted from the entire SNR is shown in Fig. 2b. The data from the two active front-illuminated CCDs (XIS0 and 3) were merged after background subtraction. The K $\alpha$  atomic lines from four Fe-peak elements (Cr, Mn, Fe, and Ni) are clearly resolved and detected at high significance. We measured their centroids and fluxes using Gaussian models, and obtained the results given in Table 1. Since the observed spectrum is dominated by metal-rich ejecta, we modeled the continuum with a bremsstrahlung representing emission from collisions between hot free electrons and highly-ionized heavy elements by using the Gaunt factor calculation method described in Kellogg et al. (1975). This model constrains the electron temperature to  $\log_{10}(T_e [\text{K}]) = 7.39 \pm 0.04$ . If a power law model is adopted instead, an unreasonably steep photon index ( $\Gamma \gtrsim 4.0$ ) is obtained, ruling out a nonthermal origin for the continuum. In fact, we found no evidence for a synchrotron X-ray filament, such as observed in young SNRs (e.g., Tycho, SN 1006), in the higher-resolution *Chandra* image of 3C 397 at the line-free energies of 4.1–5.3 keV. During the spectral analysis, we kept the absorption column density fixed at  $N_{\text{H}} = 3 \times 10^{22} \text{ cm}^{-2}$  (Safi-Harb et al. 2005) with standard Galactic abundances (Wilms et al. 2000). We repeated the analysis using different background spectra, but found no significant change in the measured values listed in Table 1.

In the non-equilibrium ionization (NEI) conditions commonly found in SNRs, line centroids and emissivities are determined by the electron temperature ( $T_e$ ) and the ionization timescale ( $n_e t$  – the product of the electron number density and plasma age, which is the time elapsed since the gas was shock-heated). To determine the plasma properties and elemental mass ratios

from the observed X-ray spectrum, we computed new atomic data based on the updated *AtomDB* database<sup>11</sup> (A. R. Foster et al., in preparation). Figure 3 shows theoretical centroid energies for the Fe-peak elements detected in the hard X-ray spectrum as a function of ionization timescale (horizontal axis) and electron temperature (vertical axis). The regions constrained by the observed spectrum are indicated in the plots. We find that the plasma conditions for the four elements overlap with one another, indicating that they originate in a single plasma component with an ionization timescale of  $\log_{10}(n_e t [\text{cm}^{-3} \text{ s}]) = 10.73 \pm 0.10$ . The K $\alpha$  line emissivities and derived mass ratios (relative to Fe) for the constrained plasma state are given in Table 1. None of the values listed there depends on the distance to the SNR. For the conditions found in 3C 397, the centroid of Fe K $\beta$  emission is predicted to be 7601<sup>+28</sup><sub>-25</sub> eV, overlapping with the measured range of the Ni K $\alpha$  centroid (see Yamaguchi et al. 2014b, for Fe K $\beta$  atomic data). This indicates that Fe K $\beta$  emission contaminates the Ni K $\alpha$  flux. Therefore, we calculated the Fe K $\beta$ /K $\alpha$  emissivity ratio, obtaining  $\varepsilon_{\text{Fe}(K\beta)}/\varepsilon_{\text{Fe}(K\alpha)} = 3.8^{+0.4}_{-0.5}\%$ . The Ni/Fe mass ratio given in Table 1 was derived taking this contribution from the Fe K $\beta$  lines into consideration.

## 3. DISCUSSION

The classification of SNRs as Type Ia or core collapse can sometimes be controversial, but the observational evidence for 3C 397 strongly favors a SN Ia origin (e.g., Chen et al. 1999; Yang et al. 2013; Yamaguchi et al. 2014a). In particular, the overall abundance pattern revealed by *Chandra* data (e.g., Fe/Mg  $\gtrsim 10$  solar, Fe/Si  $\gtrsim 3$  solar; Safi-Harb et al. 2005) is consistent with typical SN Ia yields (e.g., Iwamoto et al. 1999). Although Safi-Harb et al. (2000) did propose a core-collapse origin for this SNR, their classification was based on the high ambient density ( $\sim 1 \times 10^{-22} \text{ g cm}^{-3}$ ) estimated from the soft X-ray spectrum in *ASCA* data. This technique can yield highly uncertain results in heavily absorbed objects like 3C 397. In fact, our IR observations indicate that the ambient density is much lower (§2.1), more in line with other known Type Ia objects (Badenes et al. 2007). The IR results are also consistent with our recent systematic study of Fe K emission in SNRs, where 3C 397 is placed squarely in the SN Ia region with an ambient density less

<sup>11</sup> <http://www.atomdb.org>

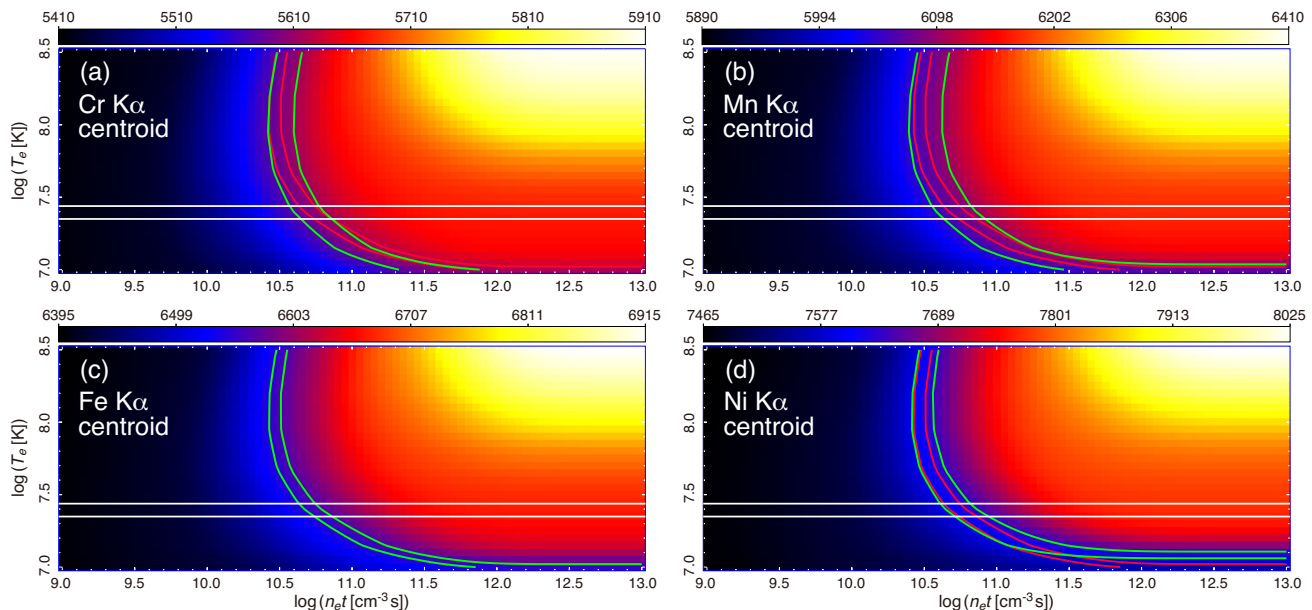


**Figure 3.** Theoretical predictions for the centroid energies of  $K\alpha$  emission from (a) Cr  $K\alpha$ , (b) Mn  $K\alpha$ , (c) Fe  $K\alpha$ , and (d) Ni  $K\alpha$ , as a function of the ionization timescale ( $n_{et}$ : horizontal axis) and electron temperature ( $T_e$ : vertical axis). The regions constrained by the observed centroid energies are indicated by the green curves. The red contours in panels (a), (b), and (d) are identical to the green contours in panel (c). The horizontal white lines indicate the electron temperature constrained by the shape of the bremsstrahlung continuum. The overlap of the contours indicates that the emission from all four lines originates in a single plasma component with an ionization timescale of  $\log_{10}(n_{et} [\text{cm}^{-3} \text{s}]) = 10.73 \pm 0.10$ . Electronic data of the centroid energies and emissivities we used are available at <http://asd.gsfc.nasa.gov/Hiroya.Yamaguchi/AtomicData/>.

than  $5 \times 10^{-24} \text{ g cm}^{-3}$  (Yamaguchi et al. 2014a).

In SNe Ia, Fe-peak nuclei are synthesized in three different burning regimes: incomplete Si burning, nuclear statistical equilibrium (NSE), and neutron-rich NSE (n-NSE). In the incomplete Si burning and NSE regimes, the yield of neutronized species (mainly stable  $^{58}\text{Ni}$  and  $^{55}\text{Mn}$  after the radioactive decays of  $^{55}\text{Co} \rightarrow ^{55}\text{Fe} \rightarrow ^{55}\text{Mn}$ ) is controlled by the pre-explosion neutron excess carried by  $^{22}\text{Ne}$  in the WD, which in turn is set mainly by the metallicity of the WD progenitor (Timmes et al. 2003; Badenes et al. 2008; Bravo 2013; Park et al. 2013). Only in the case of near- $M_{\text{Ch}}$  WDs, the innermost  $\sim 0.2 M_{\odot}$ , is consumed in the n-NSE regime (e.g., Iwamoto et al. 1999), where density-driven electron captures generate a neutron excess independently of progenitor metallicity. The Ni/Fe mass ratio found in 3C 397 (0.11–0.24, which is independent from the distance to the SNR) is, to our knowledge, the highest reported in any SN Ia observation, and it can be produced only in the n-NSE regime (and thus only in the near- $M_{\text{Ch}}$  WD) at near-solar metallicities (Fig. 2b of Park et al. 2013).

To explore the relationship between the progenitor properties and the yields of the Fe-peak elements in more detail, we calculated a grid of SN Ia explosion models with a variety of progenitor WD masses ( $M_{\text{WD}} = 0.88 M_{\odot}, 0.97 M_{\odot}, 1.06 M_{\odot}, 1.15 M_{\odot}$ , and  $M_{\text{Ch}} \approx 1.37 M_{\odot}$ ) and metallicities reasonable for Milky Way stars (Rocha-Pinto et al. 2000) ( $Z = 0.18 Z_{\odot}, 0.72 Z_{\odot}, 1.8 Z_{\odot}$ , and  $5.4 Z_{\odot}$ , where the updated value of Asplund et al. (2009) is used for  $Z_{\odot}$ ). The models were calculated with a version of the one-dimensional code described in Bravo & Martínez-Pinedo (2012), updated to include a more accurate treatment of the coupling between hydrodynamics and nuclear reactions (E.

Bravo et al., in preparation). For the  $M_{\text{Ch}}$  cases, delayed-detonation models (Khokhlov 1991) with various deflagration-to-detonation transition densities ( $\rho_{\text{DDT}}$ ) were used. The sub- $M_{\text{Ch}}$  explosions were initiated as detonations at the WD center (Sim et al. 2010), which is a good approximation for a SN Ia explosion initiated by the violent merging of binary WDs (Pakmor et al. 2012). The mass of  $^{56}\text{Ni}$  synthesized in the different models is between  $0.17 M_{\odot}$  and  $0.95 M_{\odot}$ , in agreement with the range found in normal SN Ia (Scalzo et al. 2014). As expected, the highest level of neutronization in the  $M_{\text{Ch}}$  models is achieved in the n-NSE regime. We note that this result is mainly driven by the core density of the WD, and hence one-dimensional SN Ia models should capture the fundamental trends in the synthesis of neutronized species.

In Figure 4a, the Ni/Fe and Mn/Fe mass ratios predicted by these explosion models are compared with the observed values. All the sub- $M_{\text{Ch}}$  models, regardless of progenitor mass or metallicity, fail to reproduce the high levels of neutronization found in 3C 397. We find that the  $M_{\text{Ch}}$  models can match the observed mass ratios of both Ni/Fe and Mn/Fe, but they also require relatively high metallicities. A possible interpretation for this fact is that the hot plasma component responsible for the observed K-shell emission is dominated by the n-NSE products, whereas the majority of the NSE and Si-burning products composes a lower-temperature component that is visible in the soft X-ray band (i.e., L-shell emission). An alternative is that the emission from the n-NSE region is enhanced due to density inhomogeneities in the ejecta. Otherwise, the metallicity should be indeed high. Figure 4b shows the mass ratios for the same  $M_{\text{Ch}}$  models where the values predicted for the n-NSE region (the

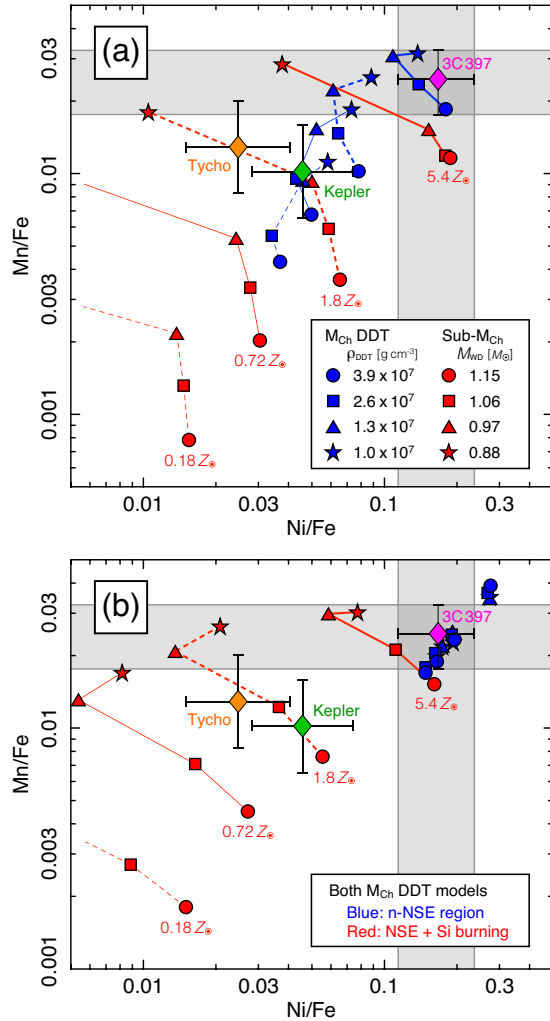


**Figure 4.** (a) Ni/Fe and Mn/Fe mass ratios in SN Ia models, compared with the observed values in 3C 397 (magenta diamond and gray regions). Blue symbols represent  $M_{\text{Ch}}$  delayed-detonation models with different values of  $\rho_{\text{DDT}}$  as indicated in the legend. Red symbols represent sub- $M_{\text{Ch}}$  detonation models with WD masses given in the legend. Models with the same progenitor metallicity are connected by lines:  $5.4 Z_{\odot}$  (thick solid),  $1.8 Z_{\odot}$  (thick dashed),  $0.72 Z_{\odot}$  (thin solid), and  $0.18 Z_{\odot}$  (thin dashed). The values for Kepler and Tycho indicated by the green and orange diamonds are calculated using the line fluxes from Park et al. (2013) and Yamaguchi et al. (2014b) with our updated atomic data. (b) Same as panel (a), but the values predicted for the innermost  $0.2 M_{\odot}$  that is dominated by the n-NSE regime (blue) and the other regions (red) from the  $M_{\text{Ch}}$  models are separately shown. The observed mass ratios for 3C 397 can be well explained by the nucleosynthesis that occurs in the n-NSE regions of standard metallicity models.

innermost  $0.2 M_{\odot}$  in our one-dimensional models) and the other regions are split. The mass ratios determined from the K-shell spectra can be well explained by the n-NSE components even with the relatively low metallicities, either alone or partially mixed with the rest of NSE matter. Since the n-NSE regime is not expected in sub- $M_{\text{Ch}}$  WDs, we can conclude that the progenitor of 3C 397 must have had a mass very close to  $M_{\text{Ch}}$ . A  $M_{\text{Ch}}$  progenitor is naturally explained by the evolution of a WD slowly accreting mass from a non-degenerate companion (e.g., Hachisu et al. 1996). Therefore, our results strongly suggest the SD scenario as the origin of this par-

ticular SN Ia. In principle,  $M_{\text{Ch}}$  or even super- $M_{\text{Ch}}$  WDs could arise in the DD scenario (Howell et al. 2006), but the properties of the galactic population of WD binaries make this a remote possibility at best (Badenes & Maoz 2012).

The large amount of neutronized material revealed by the X-ray spectrum of 3C 397 might seem exceptional in comparison to other SN Ia remnants like Kepler (Park et al. 2013) or Tycho (Yamaguchi et al. 2014b) (see Figure 4), but it is important to emphasize that 3C 397 is the only evolved Type Ia SNR that has been observed to such depth by *Suzaku*. This implies that SD progenitors might be common in the Milky Way, which is also suggested from the presence of circumstellar material confirmed in some young SN Ia remnants (e.g., Williams et al. 2011, 2012, 2014). Since the evidence in favor of DD progenitors is strong for other SNRs (González Hernández et al. 2012; Schaefer & Pagnotta 2012), it appears that both progenitor channels must contribute significantly to the SN Ia rate in star-forming galaxies.

#### 4. CONCLUSIONS

We have shown that the SN Ia progenitor of 3C 397 likely contained a WD with a mass very close to  $M_{\text{Ch}}$ . This result is anchored by the strong K-shell emission from Ni and Mn in this SNR, and is robust to the details of the data analysis and the SN nucleosynthesis calculations used to interpret the data. Other work has claimed evidence for  $M_{\text{Ch}}$  SN Ia progenitors by modeling Galactic chemical evolution (Seitenzahl et al. 2013a), or by applying phenomenological radiative transfer relations to large samples of SN Ia lightcurves (Scalzo et al. 2014), but these studies make strong assumptions about complex and highly uncertain processes. The analysis of the hard X-ray spectrum of 3C 397 presented here might be the cleanest, most robust determination of the mass of a single SN Ia progenitor to date, and strongly suggests an SD progenitor for this particular remnant. Future deep observations with higher angular/spectral resolution including the soft X-ray band will allow us to investigate the spatial distribution of the elemental mass ratios and plasma properties (i.e., electron temperature and density). This will help understand why the NSE and Si-burning products are little visible in the hard X-ray band (see §3), and constrain the detailed explosion mechanism of  $M_{\text{Ch}}$  SNe Ia as well as the dynamical evolution of their remnants.

We thank Drs. Ken'ichi Nomoto, Samar Safi-Harb, Randall K. Smith, and Michael C. Witthoeft for helpful discussion and suggestions. E.B. is supported by Spanish MINECO grant AYA2013-40545. Japanese authors acknowledge financial support by JSPS Grant-in-Aid for Scientific Research numbers 23740141/26800100 (K.M.), 24740123 (M.N.), and 23000004/24540229 (K.K).

#### REFERENCES

- Asplund, M., Grevesse, N., Sauval, A. J., & Scott, P. 2009, *ARA&A*, 47, 481  
 Badenes, C., Bravo, E., & Hughes, J. P. 2008, *ApJ*, 680, L33

- Badenes, C., Hughes, J. P., Bravo, E., & Langer, N. 2007, *ApJ*, 662, 472
- Badenes, C., & Maoz, D. 2012, *ApJ*, 749, L11
- Borkowski, K. J., Williams, B. J., Reynolds, S. P., et al. 2006, *ApJ*, 642, L141
- Bravo, E. 2013, *A&A*, 550, A24
- Bravo, E., & Martínez-Pinedo, G. 2012, *Phys. Rev. C*, 85, 055805
- Chen, Y., Sun, M., Wang, Z.-R., & Yin, Q. F. 1999, *ApJ*, 520, 737
- Dessart, L., Hillier, D. J., Blondin, S., & Khokhlov, A. 2014, *MNRAS*, 441, 3249
- Gerardy, C. L., Meikle, W. P. S., Kotak, R., et al. 2007, *ApJ*, 661, 995
- González Hernández, J. I., Ruiz-Lapuente, P., Tabernero, H. M., et al. 2012, *Nature*, 489, 533
- Hachisu, I., Kato, M., & Nomoto, K. 1996, *ApJ*, 470, L97
- Howell, D. A., Sullivan, M., Nugent, P. E., et al. 2006, *Nature*, 443, 308
- Iwamoto, K., Brachwitz, F., Nomoto, K., et al. 1999, *ApJS*, 125, 439
- Kellogg, E., Baldwin, J. R., & Koch, D. 1975, *ApJ*, 199, 299
- Khokhlov, A. M. 1991, *A&A*, 245, 114
- Li, W., Bloom, J. S., Podsiadlowski, P., et al. 2011, *Nature*, 480, 348
- Maeda, K., Röpke, F. K., Fink, M., et al. 2010a, *ApJ*, 712, 624
- Maeda, K., Taubenberger, S., Sollerman, J., et al. 2010b, *ApJ*, 708, 1703
- Maoz, D., Mannucci, F., & Nelemans, G. 2014, *ARA&A*, 52, 107
- Mazzali, P. A., Röpke, F. K., Benetti, S., & Hillebrandt, W. 2007, *Science*, 315, 825
- Ozawa, M., Uchiyama, H., Matsumoto, H., et al. 2009, *PASJ*, 61, 1
- Pakmor, R., Kromer, M., Taubenberger, S., et al. 2012, *ApJ*, 747, L10
- Park, S., Badenes, C., Mori, K., et al. 2013, *ApJ*, 767, L10
- Patat, F., Chandra, P., Chevalier, R., et al. 2007, *Science*, 317, 924
- Perlmutter, S., Aldering, G., Goldhaber, G., et al. 1999, *ApJ*, 517, 565
- Riess, A. G., Filippenko, A. V., Challis, P., et al. 1998, *AJ*, 116, 1009
- Rocha-Pinto, H. J., Maciel, W. J., Scalo, J., & Flynn, C. 2000, *A&A*, 358, 850
- Safi-Harb, S., Dubner, G., Petre, R., Holt, S. S., & Durouchoux, P. 2005, *ApJ*, 618, 321
- Safi-Harb, S., Petre, R., Arnaud, K. A., et al. 2000, *ApJ*, 545, 922
- Scalzo, R. A., Ruiter, A. J., & Sim, S. A. 2014, *MNRAS*, 445, 2535
- Schaefer, B. E., & Pagnotta, A. 2012, *Nature*, 481, 164
- Seitenzahl, I. R., Cescutti, G., Röpke, F. K., Ruiter, A. J., & Pakmor, R. 2013a, *A&A*, 559, L5
- Seitenzahl, I. R., Ciaraldi-Schoolmann, F., Röpke, F. K., et al. 2013b, *MNRAS*, 429, 1156
- Seitenzahl, I. R., Summa, A., Krauß, F., et al. 2015, *MNRAS*, 447, 1484
- Sim, S. A., Röpke, F. K., Hillebrandt, W., et al. 2010, *ApJ*, 714, L52
- Sternberg, A., Gal-Yam, A., Simon, J. D., et al. 2011, *Science*, 333, 856
- Timmes, F. X., Brown, E. F., & Truran, J. W. 2003, *ApJ*, 590, L83
- Truelove, J. K., & McKee, C. F. 1999, *ApJS*, 120, 299
- van Kerkwijk, M. H. 2013, *Royal Society of London Philosophical Transactions Series A*, 371, 20236
- Webbink, R. F. 1984, *ApJ*, 277, 355
- Weingartner, J. C., & Draine, B. T. 2001, *ApJ*, 548, 296
- Whelan, J., & Iben, Jr., I. 1973, *ApJ*, 186, 1007
- Williams, B. J., Borkowski, K. J., Reynolds, S. P., et al. 2012, *ApJ*, 755, 3
- Williams, B. J., Blair, W. P., Blondin, J. M., et al. 2011, *ApJ*, 741, 96
- Williams, B. J., Borkowski, K. J., Reynolds, S. P., et al. 2014, *ApJ*, 790, 139
- Wilms, J., Allen, A., & McCray, R. 2000, *ApJ*, 542, 914
- Yamaguchi, H., Badenes, C., Petre, R., et al. 2014a, *ApJ*, 785, L27
- Yamaguchi, H., Eriksen, K. A., Badenes, C., et al. 2014b, *ApJ*, 780, 136
- Yang, X. J., Tsunemi, H., Lu, F. J., et al. 2013, *ApJ*, 766, 44